PHYTOplankton biomass and diversity Climate Change Initiative (PHYTO-CCI)

ESA 4000147645/25/I-LR
D2.3 End-to-End ECV Uncertainty Budget (E3UB)

Project led by

PML | Plymouth Marine Laboratory

In cooperation with

CNR ISMAR ISTITUTO DI SCIENZE MARINE

AWI

Brockmann Consult

The Danish Meteorological Institute

University of Exeter

FCiências[ID] Associação para a Investigação e Desenvolvimento de Ciências

Document properties

Project:	PHYTO-CCI
Document title:	End-to-End ECV Uncertainty Budget (E3UB)
Reference:	D2.3
Date:	27/07/2026
Version:	1.1

Science leads: Gemma Kulk & Victor Martinez-Vicente – PML

Reviewed: Lianne Jackson – PML

Sarah Connors – ESA

Digitally signed by Sarah Connors
Date: 2026.07.28 09:02:25 +01'00'

Address: Plymouth Marine Laboratory (PML)
Prospect Place
The Hoe
Plymouth
PL1 2DH
United Kingdom
Tel: +44 (0)1752 633100

Copyright: © Plymouth Marine Laboratory 2026. The copyright in this document is vested in Plymouth Marine Laboratory. This document may only be reproduced in whole or in part, or stored in a retrieval system, or transmitted in any form, or by any means electronic, mechanical, photocopying or otherwise, either with the prior permission of Plymouth marine Laboratory or in accordance with the terms of ESA Contract No. 4000147645/25/I-LR.

Document version history

Version	Date	Author(s) / Contributor(s)	Comment
1.0 (draft)	17/12/2025	Gemma Kulk	Template
1.0 (draft)	10/06/2026	Ralf Quast, Gemma Kulk	First draft
1.0	12/06/2026	Ralf Quast, Gemma Kulk, Peter Miller, Salem I. Salem	First release
1.1	27/07/2026	Ralf Quast, Gemma Kulk	Description of sources of uncertainty was added and results were updated following correction to one phytoplankton carbon algorithm

Index

1 Introduction

1.1 Purpose of document

This End-to-End ECV Uncertainty Budget (E3UB) details the approach to uncertainty characterisation of the PHYTOplankton biomass and diversity Climate Change Initiative (PHYTO-CCI). As a first step in the development of the Essential Climate Variable (ECV) dataset for phytoplankton biomass and diversity, the approach to error-characterisation of the Ocean Colour Climate Change (OC-CCI) is followed in which optical water types are used to assign per-pixel uncertainties. Further developments look towards incorporating a formal error propagation method.

1.2 Structure

The E3UB describes the methods for uncertainty estimation following an optical water class approach for the phytoplankton carbon biomass and pigment diversity data products in Section 2. Uncertainties for each optical water class for the phytoplankton carbon and pigment algorithms are reported in Section 3. Recommendations to users and the validation team are provided in Section 4. Future developments of uncertainty characterisation are described in Section 5. The references are provided in Section 6.

1.3 Related documents

Documents related to the PHYTO-CCI E3UB are the PHYTO-CCI Product Validation and Algorithm Selection Report (PVASR), Algorithm Theoretical Baseline Document (ATBD) and Algorithm Development Plan (ADP).

2 Methods

2.1 Optical Water Class approach

The algorithm blending approach developed by Jackson *et al.* (2017) for the Ocean Colour Climate Change Initiative (OC-CCI) addresses a fundamental challenge in satellite oceanography: no single bio-optical algorithm can accurately retrieve chlorophyll-a concentration (chl-a) across all natural waters. Instead of applying a rigid global empirical model, the Jackson *et al.* framework utilises an Optical Water Type (OWT) classification system. The classification scheme relies on a set of 14 distinct OWTs. These classes define a spectral continuum ranging from highly oligotrophic, clear open-ocean waters (Classes 1–6), through moderately productive and diatom-dominated waters (Classes 7–10), to highly turbid, sediment-dominated, or eutrophic coastal and inland waters (Classes 11–14). The classification is performed on a per-pixel basis by comparing the satellite-derived remote sensing reflectance $\boldsymbol{R}_{\mathrm{rs}} \in \mathbb{R}^n$ ($\mathbb{R}^n$ is the spectral vector space of remote sensing reflectance with n measured spectral wavebands) against the predefined mean spectral signatures of these 14 target classes. Table 1 summarises the relevant water classes in terms of class set means and their standard deviations. Figure 1 illustrates the water classes graphically.

Table 1. Water class set means and standard deviations in terms of remote sensing reflectance for the OC-CCI band set. Figures in parentheses represent the standard deviation. Abbreviations: OWT = Optical water type.

Spectral signatures of water classes (sr^{-1})						
OWT	**412 nm**	**443 nm**	**490 nm**	**510 nm**	**555 nm**	**670 nm**
1	0.01871 (441)	0.01344 (110)	0.00734 (145)	0.00361 (177)	0.00153 (211)	0.00017 (87)0
2	0.01583 (80)0	0.01182 (59)0	0.00691 (89)0	0.00351 (114)	0.00150 (133)	0.00015 (54)0
3	0.01345 (77)0	0.01049 (58)0	0.00657 (103)	0.00348 (134)	0.00155 (158)	0.00016 (63)0
4	0.01106 (76)0	0.00908 (60)0	0.00617 (107)	0.00348 (142)	0.00163 (168)	0.00018 (69)0
5	0.00914 (68)0	0.00765 (51)0	0.00566 (81)0	0.00340 (103)	0.00168 (115)	0.00019 (40)0
6	0.00759 (56)0	0.00652 (44)0	0.00520 (63)0	0.00331 (82)0	0.00172 (88)0	0.00021 (28)0
7	0.00605 (59)0	0.00555 (43)0	0.00475 (65)0	0.00324 (86)0	0.00180 (95)0	0.00023 (30)0
8	0.00471 (53)0	0.00465 (38)0	0.00421 (51)0	0.00304 (67)0	0.00179 (70)0	0.00024 (21)0
9	0.00353 (52)0	0.00375 (40)0	0.00368 (50)0	0.00291 (67)0	0.00192 (90)0	0.00028 (30)0
10	0.00244 (57)0	0.00285 (44)0	0.00307 (41)0	0.00257 (50)0	0.00184 (86)0	0.00029 (33)0
11	0.00111 (55)0	0.00166 (56)0	0.00217 (54)0	0.00200 (47)0	0.00168 (62)0	0.00030 (33)0
12	0.00336 (193)	0.00390 (175)	0.00556 (182)	0.00615 (166)	0.00746 (227)	0.00215 (206)
13	0.00642 (369)	0.00746 (301)	0.01032 (291)	0.01099 (247)	0.01250 (341)	0.00443 (455)
14	0.00988 (248)	0.01245 (278)	0.01835 (425)	0.01988 (451)	0.02286 (616)	0.00729 (583)

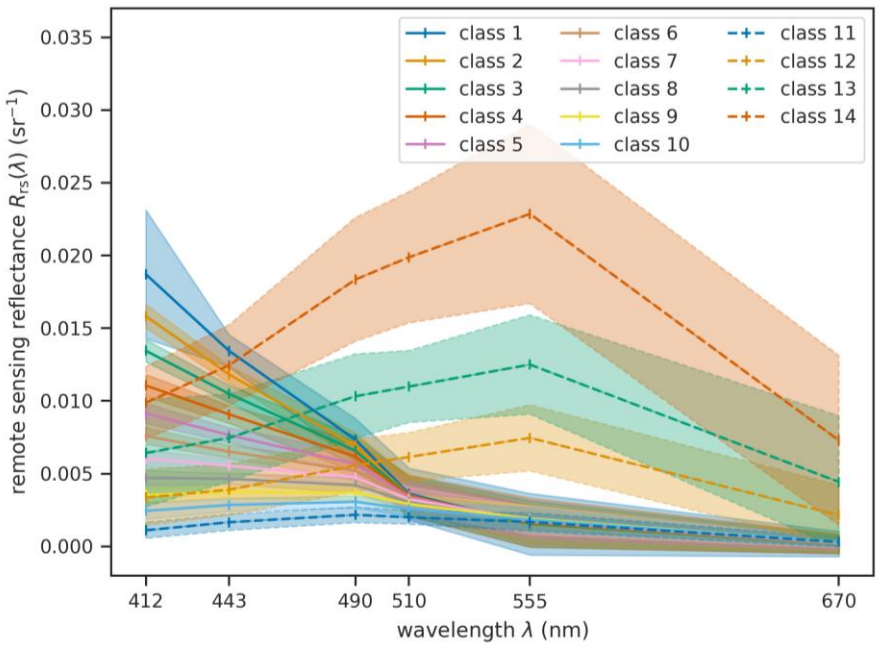

Figure 1. Spectral signatures of water classes. Lines show the class means and shaded regions illustrate the standard deviation.

Rather than forcing a hard mathematical switch between algorithms, which introduces artificial boundaries and severe spatial discontinuities in satellite imagery, the Jackson *et al.* (2017) approach utilises fuzzy logic. For every individual pixel, the Mahalanobis distance between the observed $R_{\mathrm{rs}}(\lambda)$ spectrum and the mean spectrum of each of the OWTs is calculated. Let $\boldsymbol{R}_{\mathrm{rs},k} \in \mathbb{R}^n$ denote the water class mean remote sensing reflectance (see Table 1) and let $\mathbf{C}_k \in \mathbb{R}^{n\times n}$ denote the covariance matrix of water class k. Further let $\boldsymbol{A}_k = \boldsymbol{R}_{\mathrm{rs}} - \boldsymbol{R}_{\mathrm{rs},k}$ denote the difference between observed and class mean remote sensing reflectance. Then the squared Mahalanobis distance is:

$$d_k^2 = (\boldsymbol{A}_k\,, \mathbf{C}_k^{-1}\boldsymbol{A}_k\,)$$

Where "$(\cdot,\cdot)$" denotes the inner product in $\mathbb{R}^n$. This squared distance is converted into a membership grade w_k, ranging smoothly from 0 (no similarity) to 1 (perfect match):

$$w_k = 1 - \frac{\gamma\left(\frac{n}{2}, \frac{d_k^2}{2}\right)}{\Gamma\left(\frac{n}{2}\right)}$$

where $\Gamma(s) = \int_0^\infty t^{s-1}e^{-t}\mathrm{d}t$ and $\gamma(s,x) = \int_0^x t^{s-1}e^{-t}\mathrm{d}t$ denote the complete gamma function and the lower incomplete gamma function, respectively. The sum of all membership grades for a single pixel is unconstrained, i.e., the sum of all grades is usually not unity. OC-CCI runs multiple underlying chl-a algorithms. For clear and open waters, standard band-ratio algorithms (such as the NASA OCX scheme) are computed. For turbid or complex Case-2 waters, alternative algorithms are executed. The final (common logarithm of) the chl-a value for the pixel, x_w, is derived as the weighted average of the outputs x_k from the algorithm selected for each water class k, using the fuzzy membership grades as the weighting coefficients:

$$x_w = \frac{\sum_k x_k w_k}{\sum_k w_k}$$

Because chl-a serves as the primary input for satellite-based phytoplankton carbon models, quantifying the input uncertainty propagation is vital. The Jackson *et al.* (2017) approach provides a foundation for this uncertainty budget in two distinct ways:

1) **Per-pixel mapping:** Prior to this framework, satellite products often applied a single, uniform root-mean-square error globally. The Jackson *et al.* (2017) method maps validation-derived uncertainty (expressed in terms of root-mean-square errors Δ_k and biases m_k) directly to each OWT. The final uncertainty for any given pixel is calculated by blending these class-specific errors using the same fuzzy membership weights:

$$\Delta_w = \frac{\sum_k \Delta_k w_k}{\sum_k w_k}\,, \qquad m_w = \frac{\sum_k m_k w_k}{\sum_k w_k}$$

2) **Elimination of structural noise:** By smoothing the transitions between coastal and open-ocean algorithms, the framework prevents artificial spatial gradients. This ensures that variations in downstream phytoplankton carbon calculations reflect ecological boundaries rather than mathematical artifacts introduced by algorithm switching.

The optical water type approach to uncertainty quantification mainly accounts for representation errors that only occur at the comparison interface to *in situ* measurements of water properties (Bulgin *et al.*, 2022). Consequently, it ignores the quantification and propagation of uncertainties arising from remote sensing radiometry, atmospheric correction and in-water radiative transfer calculations completely. Thus, the optical water type approach quantifies only one isolated contribution to the full uncertainty budget, which is, moreover, only meaningful when the quantity measured by field measurements defines the measurand. We denote this per-pixel **representation uncertainty** by:

$$u_\mathrm{r}^2(x_w) = \Delta_w^2 - m_w^2$$

Here, the representation uncertainty represents the dispersion of uncorrelated random errors that remain, after the bias correction m_w was applied to the retrieved value x_w. It is worth noting that pixel memberships themselves are uncertain because class means and covariances are uncertain. However, since the purpose of this document is to establish a formal uncertainty propagation framework by means of the GUM uncertainty framework (JCGM, 2023), quantifying the uncertainty of pixel memberships as a component of the representation uncertainty is not considered further within the scope of this document.

Representation uncertainty is sometimes referred to as diagnostic uncertainty, which does not describe the nature of the uncertainty; in fact, all uncertainties are diagnostic tools. The strict metrological term is representation uncertainty.

2.2 Application to phytoplankton carbon and pigment algorithms

The optical water class approach, originally designed for ocean colour chl-a algorithms, is applied to phytoplankton carbon and pigment algorithms to calculate weighted statistics and uncertainties. This methodology employs fuzzy class membership grades, denoted as $w_{k,i}$, to determine the root-mean-square difference (Δ_k) and bias (m_k) for each water class, facilitating a comprehensive assessment of both spectral and representation uncertainties.

Let $x_{\mathrm{f},i}$ and $x_{\mathrm{s},i}$ denote the common logarithm of field (*in situ*) and space-based measurements of phytoplankton carbon or pigment concentration, respectively, and let N denote the number of space-to-field match-ups. Then the root-mean-square-difference and bias for each water class k are given by:

$$\Delta_k = \sqrt{\frac{\sum_{i=1}^{N} w_{k,i}\left(x_{\mathrm{s},i} - x_{\mathrm{f},i}\right)^2}{\sum_{i=1}^{N} w_{k,i}}}\,, \qquad m_k = \frac{\sum_{i=1}^{N} w_{k,i}\left(x_{\mathrm{s},i} - x_{\mathrm{f},i}\right)}{\sum_{i=1}^{N} w_{k,i}}$$

The purely statistical standard uncertainty of the bias for each water class depends on the effective sample size N_{eff} and is given by:

$$u^2(m_k) = \frac{\sum_{i=1}^{N} w_{k,i}\left(\left(x_{\mathrm{s},i} - x_{\mathrm{f},i}\right) - m_k\right)^2}{\left(N_{\mathrm{eff}} - 1\right)\sum_{i=1}^{N} w_{k,i}}\,, \qquad N_{\mathrm{eff}} = \frac{\left(\sum_{i=1}^{N} w_{k,i}\right)^2}{\sum_{i=1}^{N} w_{k,i}^2}$$

According to the law of propagation of uncertainty, the standard uncertainties of the water class biases must be propagated, when a bias correction is applied to a blended phytoplankton carbon or pigment concentration:

$$u_{\mathrm{r}}^2(x_w - m_w) = \Delta_w^2 - m_w^2 + u^2(m_w)\,, \qquad u^2(m_w) = \frac{\sum_k w_k^2 u^2(m_k)}{\left(\sum_k w_k\right)^2}$$

Consequently, applying a bias correction increases the standard uncertainty of the phytoplankton product, despite improving its overall accuracy.

3 Results

The intercomparison of phytoplankton carbon biomass and pigment diversity algorithms in the first development round of the PHYTO-CCI project provided the bias and root-mean-square-difference for all algorithms and across all OWTs that is needed to estimate per-pixel uncertainties following the methods described in Section 2. A detailed description of each algorithm and the results of the intercomparison can be found in the Algorithm Theoretical Baseline Document (ATBD) and the Product Validation and Algorithm Selection Report (PVASR). Here we describe the results of the application of the OWT approach to uncertainty estimation for the phytoplankton carbon Algorithms A (Bellacicco *et al.*, 2020; Zhang *et al.*, 2024), B_1 and B_2 (Kostadinov *et al.* 2023), C (Marañón *et al.*, 2014) and D (Sathyendranath *et al.*, 2020) and for the phytoplankton pigment Algorithm B_2 (Li *et al.*, 2023).

3.1 Per water-class uncertainties for phytoplankton carbon biomass

To derive the per-pixel uncertainties for the phytoplankton carbon algorithms, we used the bias (m_k) and root-mean square-difference (Δ_k) for each OWT as reported in Table 2. These statistical metrics were derived from Comparison 2, in which additional quality control was applied to the *in situ* – satellite match-up dataset that was used to intercompare the phytoplankton carbon algorithms. This combination of data resulted in the best performance across all algorithms (see PVASR for details). It is noted that the bias and root-mean-square-differences could not be computed for OWT 13 and 14, as there was an insufficient amount of datapoints available for these water types (i.e., between 4–7 datapoints for OWT 13 and 0–1 for OWT 14, depending on the specific algorithm). For these two water types, we assumed that the bias and root-mean-square-difference was the same as for OWT 12, which has the closed optical signature (Figure 1). As described in the PVASR, most of the phytoplankton carbon algorithms showed negative bias when all OWTs were considered and changed from negative to positive biases from optically clear to complex waters (i.e., from low to high OWT; Table 2). The exception is Algorithm B_1, which is a tuned version of the algorithm developed by Kostadinov *et al.* (2023) and showed positive bias across all OWTs. The root-mean-square-difference ranged between 0.13 and 0.86 for all algorithms and across OWTs and was lowest in Algorithm B_1.

*Table 2. Bias (m_k), root-mean-square-difference (Δ_k) and number of observations (N) for the five phytoplankton carbon algorithms for all match-up data and for match-up data within the dominant optical water type (k). Note that results are from Comparison 2 (see PVASR) and insufficient data points were available to obtain the statistical metrics for OWT 13 and 14 (indicated by *). Values are given in log10 mg C m^{-3} for the bias and root-mean-square-difference.*

Algorithm A				Algorithm B_1				Algorithm B_2			
k	m_k	Δ_k	N	k	m_k	Δ_k	N	k	m_k	Δ_k	N
all	-0.24	0.42	9,569	all	0.09	0.22	8,733	all	-0.20	0.48	8,733
1	-0.52	0.67	423	1	0.15	0.25	435	1	-0.54	0.62	435
2	-0.32	0.40	2,642	2	0.03	0.13	2,459	2	-0.48	0.53	2,459
3	-0.27	0.41	2,411	3	0.08	0.18	2,154	3	-0.30	0.40	2,154
4	-0.21	0.40	969	4	0.11	0.24	900	4	-0.10	0.35	900
5	-0.34	0.60	635	5	0.16	0.27	455	5	-0.42	0.56	455
6	-0.16	0.32	831	6	0.08	0.24	757	6	-0.01	0.28	757
7	-0.09	0.42	98	7	0.16	0.26	77	7	0.23	0.37	77
8	0.03	0.44	328	8	0.18	0.34	307	8	0.45	0.59	307
9	-0.10	0.26	762	9	0.11	0.24	690	9	0.19	0.35	690
10	0.34	0.59	51	10	0.26	0.39	65	10	0.60	0.67	65
11	0.20	0.45	368	11	0.26	0.40	368	11	0.76	0.82	368
12	0.04	0.50	50	12	0.17	0.38	62	12	0.80	0.86	62
13*	0.04	0.50	50	13*	0.17	0.38	62	13*	0.80	0.86	62
14*	0.04	0.50	50	14*	0.17	0.38	62	14*	0.80	0.86	62

Table 2. Continued.

Algorithm C			
k	m_k	Δ_k	N
all	-0.11	0.26	9,775
1	-0.23	0.31	457
2	-0.27	0.29	2,646
3	-0.14	0.21	2,457
4	-0.07	0.21	980
5	-0.19	0.28	661
6	-0.02	0.23	818
7	0.02	0.17	105
8	0.13	0.33	335
9	0.07	0.21	736
10	0.33	0.42	64
11	0.25	0.40	418
12	0.20	0.41	90
13*	0.20	0.41	90
14*	0.20	0.41	90

Algorithm D			
k	m_k	Δ_k	N
all	-0.33	0.43	9,754
1	-0.48	0.54	454
2	-0.49	0.52	2,642
3	-0.36	0.42	2,454
4	-0.27	0.36	980
5	-0.39	0.48	660
6	-0.17	0.33	817
7	-0.11	0.32	104
8	-0.13	0.37	335
9	-0.09	0.30	734
10	0.11	0.36	62
11	-0.07	0.37	417
12	-0.13	0.42	87
13*	-0.13	0.42	87
14*	-0.13	0.42	87

The application of the OWT approach to uncertainty estimation resulted in mapped products of the bias and root-mean-square-difference for each phytoplankton carbon algorithm (Figure 2), revealing spatial patterns in these statistical metrics. For May 2010, chosen here as an example month, the bias in Algorithm A, B_2, C and D was higher in the tropics and at higher latitudes and lower in the open oceans at mid-latitudes. For Algorithm B_1, a similar spatial distribution was observed, but the bias is positive for all pixels (Figure 2C). The spatial distribution of the bias is closely related to that of the phytoplankton carbon concentration, and relatively higher biases are observed in a smaller number of pixels at higher latitudes and in the tropics (data not shown). The root-mean-square-difference showed a more uniform distribution, but higher values were observed at higher latitudes in all algorithms and in the open ocean gyres in Algorithms A, B_2, C and D, but not in Algorithm B_1 (Figure 2). From the bias and root-mean-square-difference, the standard deviation and standard error of the mean can be calculated as measures of uncertainty (also see Section 2), with the latter also incorporating the number of observations for each individual pixel (derived from OC-CCI). For the example month described here, the global mean standard deviation ranged between 22-93% and the standard error of the mean ranged between 6.3-9.2%, with Algorithm C having the lowest uncertainty (data not shown).

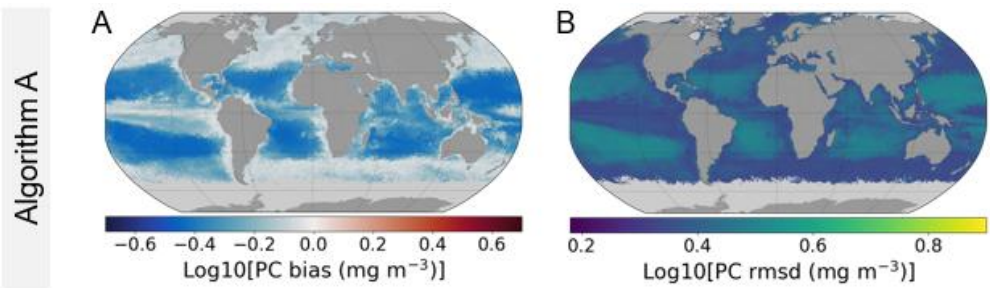

Figure 2. Example of bias and root-mean-square-difference (rmsd) in phytoplankton carbon from algorithm A (A-B), algorithm B_1 (C-D), algorithm B_2 (E-F), algorithm C (G-H) and algorithm D (I-J) for May 2010. Bias and rmsd were assigned per-pixel using optical water types from OC-CCI using the information provided in Table 2. See Section 2 for a detailed description of the method.

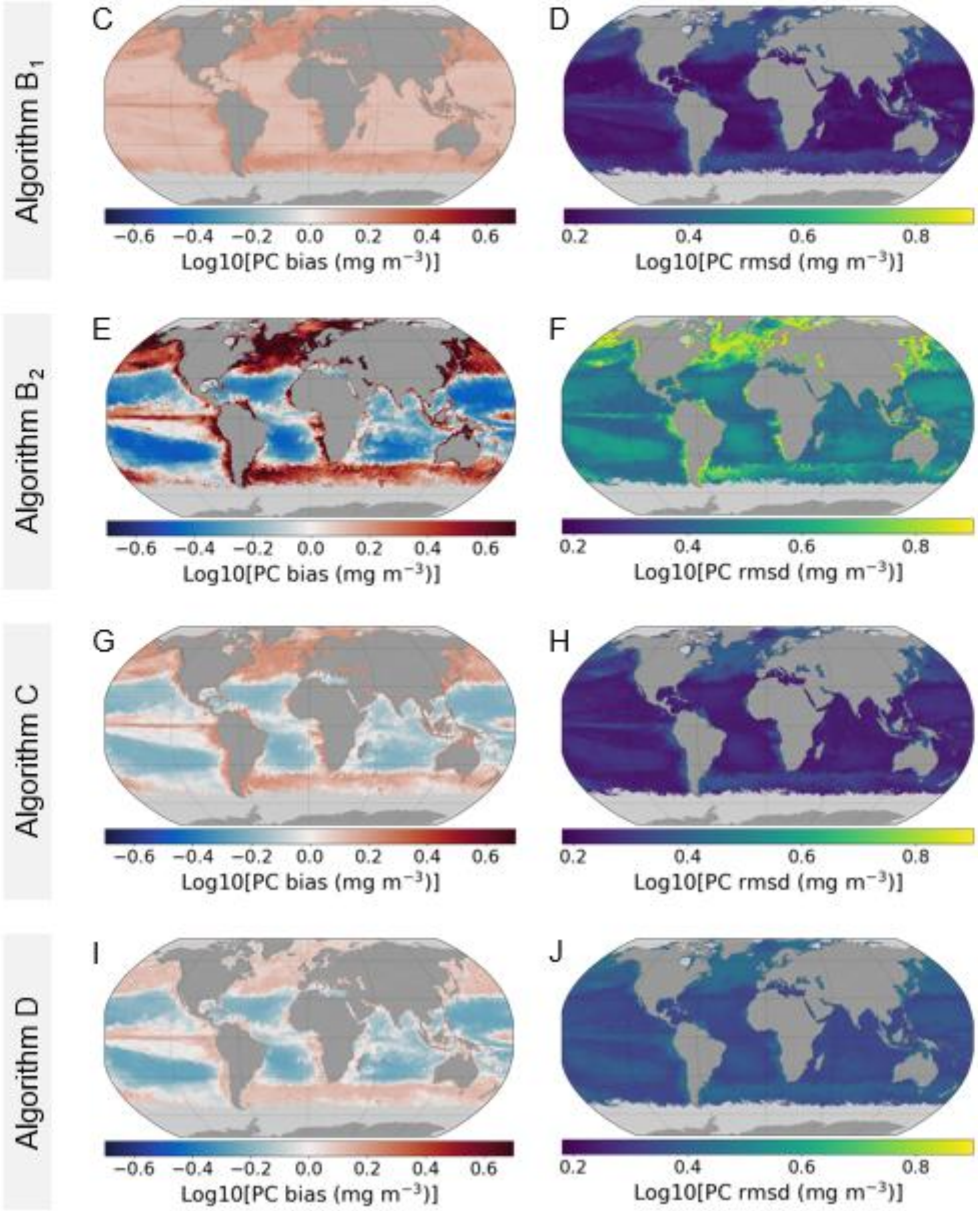

Figure 2. Continued.

3.2 Per water-class uncertainties for phytoplankton pigment diversity

For phytoplankton pigments, we used the bias and root-mean-square-difference of Algorithm B_2 (Li *et al.*, 2023) that was selected for production of the first global pigment dataset in PHYTO-CCI following the results of the intercomparison (Table 3; also see PVASR). This algorithm estimates nine different pigments, including 19'-butanoyloxyfucoxanthin, 19'-hexanoyloxyfucoxanthin, alloxanthin, total chlorophyll-a, divinyl chlorophyll-a, total chlorophyll-b, fucoxanthin, peridinin and zeaxanthin, and per-pixel uncertainties were estimated for each pigment following the OWT approach described in Section 2. In general, bias was relatively low for all pigments and varied between negative and positive biases depending on the OWT and specific pigment (Table 3). The root-mean-square-difference ranged between 0.13 and 0.69 and was overall lowest for the total chlorophyll-a concentration. It is noted that for all pigments insufficient data was available to derive statistical metrics for OWTs 1 and 7, with some pigments also missing data for other OWTs, and the bias and root-mean-square-difference were assigned according to the optically closest water type.

Table 3. Bias (m_k), root-mean-square-difference (Δ_k) and number of observations (N) for the phytoplankton pigment Algorithm B_2 (Li et al.*, 2023) for all match-up data and for match-up data within each dominant optical water type (k) (also see PVASR). For some pigments, insufficient data points were available to obtain the statistical metrics for specific optical water types as indicated by *. Values are given in log10 mg C m^{-3} for the bias and root-mean-square-difference.*

19'-Butanoyloxyfucoxanthin			
k	m_k	Δ_k	N
all	0.03	0.26	828
1*	0.04	0.20	49
2	0.04	0.20	49
3	-0.01	0.16	75
4	-0.01	0.27	59
5	0.02	0.15	55
6	-0.08	0.31	35
7*	0.04	0.28	116
8	0.04	0.28	116
9	0.01	0.22	150
10	0.14	0.33	31
11	-0.03	0.29	130
12	0.04	0.23	81
13	-0.09	0.43	35
14*	-0.09	0.43	35

19'-Hexanoyloxyfucoxanthin			
k	m_k	Δ_k	N
all	0.03	0.27	883
1*	0.08	0.16	54
2	0.08	0.16	54
3	0.05	0.15	77
4	0.03	0.19	64
5	0.07	0.15	60
6	-0.07	0.40	36
7*	0.05	0.31	123
8	0.05	0.31	123
9	-0.04	0.28	160
10	0.12	0.20	31
11	0.00	0.31	136
12	0.02	0.34	81
13	0.06	0.43	43
14	0.26	0.46	11

Alloxanthin			
k	m_k	Δ_k	N
all	0.16	0.41	487
1*	0.11	0.20	20
2*	0.11	0.20	20
3*	0.11	0.20	20
4	0.11	0.20	20
5*	-0.07	0.26	11
6	-0.07	0.26	11
7	0.24	0.50	80
8	0.24	0.50	80
9	0.15	0.29	81
10	0.40	0.52	11
11	0.14	0.48	114
12	0.19	0.41	70
13	0.22	0.38	40
14	0.05	0.30	13

Chlorophyll-a			
k	m_k	Δ_k	N
all	0.02	0.19	901
1*	0.01	0.14	54
2	0.01	0.14	54
3	-0.01	0.13	77
4	-0.02	0.20	64
5	0.03	0.16	60
6	0.00	0.26	37
7*	-0.01	0.19	123
8	-0.01	0.19	123
9	0.00	0.15	160
10	0.03	0.09	31
11	-0.01	0.25	140
12	0.04	0.21	86
13	0.08	0.24	46
14	0.09	0.36	16

Chlorophyll-a_2			
k	m_k	Δ_k	N
all	0.05	0.27	249
1*	0.09	0.35	20
2	0.09	0.35	20
3	0.03	0.21	50
4	0.12	0.27	21
5	0.00	0.13	24
6	0.02	0.41	16
7*	0.01	0.37	29
8	0.01	0.37	29
9	-0.01	0.31	50
10	0.23	0.33	13
11*	0.23	0.33	13
12	0.10	0.30	14
13*	0.10	0.30	14
14*	0.10	0.30	14

Chlorophyll-b			
k	m_k	Δ_k	N
all	-0.01	0.28	753
1*	-0.02	0.21	43
2	-0.02	0.21	43
3	0.04	0.23	53
4	-0.04	0.24	46
5	-0.08	0.37	48
6	-0.02	0.28	34
7*	-0.04	0.29	109
8	-0.04	0.29	109
9	-0.02	0.24	132
10	0.22	0.43	27
11	-0.08	0.29	127
12	0.04	0.26	79
13	-0.02	0.23	39
14	0.07	0.31	13

Table 3. Continued.

Fucoxanthin				**Peridinin**				**Zeaxanthin**			
k	m_k	Δ_k	N	k	m_k	Δ_k	N	k	m_k	Δ_k	N
all	0.01	0.29	862	all	0.06	0.35	660	all	0.03	0.27	841
1*	0.08	0.18	47	1*	-0.04	0.17	37	1*	0.01	0.14	54
2	0.08	0.18	47	2	-0.04	0.17	37	2	0.01	0.14	54
3	0.01	0.19	72	3	0.01	0.15	45	3	0.02	0.14	77
4	0.05	0.27	59	4	0.02	0.27	38	4	0.03	0.17	63
5	0.04	0.24	54	5	0.00	0.15	41	5	-0.08	0.30	59
6	0.00	0.32	35	6	0.02	0.25	28	6	0.04	0.14	37
7*	-0.06	0.33	119	7*	0.11	0.31	103	7*	-0.03	0.31	119
8	-0.06	0.33	119	8	0.11	0.31	103	8	-0.03	0.31	119
9	-0.03	0.30	152	9	0.07	0.27	112	9	0.04	0.22	150
10	0.02	0.27	31	10	0.51	0.69	18	10	0.04	0.13	29
11	-0.05	0.32	139	11	0.05	0.47	117	11	0.00	0.31	126
12	-0.04	0.30	86	12	0.07	0.38	72	12	0.05	0.35	67
13	0.10	0.27	46	13	0.07	0.38	36	13	-0.14	0.42	40
14	0.24	0.69	16	14*	0.07	0.38	36	14	0.18	0.47	14

The spatial distribution of the bias and root-mean-square-difference varied for individual pigments (Figure 3). For example month May 2010, the bias was higher in open ocean gyres in 19'-butanoyloxyfucoxanthin, 19'-hexanoyloxyfucoxanthin, fucoxanthin and the total chlorophyll-a concentration (Figures 3A, 3C, 3G, 3M), all pigments that are typically associated with larger phytoplankton species, including diatoms. For the other pigments, bias was typically higher at high latitudes and in the tropics around the equator (Figures 3E, 3I, 3K, 3O, 3Q). It is also notable that some pigments showed positive bias globally, i.e., 19'-butanoyloxyfucoxanthin, 19'-hexanoyloxyfucoxanthin, alloxanthin and divinyl chlorophyll-a, whereas the other pigments showed both positive and negative biases (Figure 3). The bias was highest at higher latitudes for alloxanthin and peridinin (Figures 3E, 3O). The root-mean-square-difference seems to have a similar spatial distribution for all pigments, with higher values in the tropics and at higher latitudes (Figure 3). Similar to the bias, the root-mean-square-difference is highest for alloxanthin and peridinin at higher latitudes (Figures 3F, 3P). The observed spatial distribution in the bias and root-mean-square-difference are closely related to the specific pigment concentration and relative errors are highest in the North Pacific Ocean, around the equator and in the Southern Ocean (data not shown). The global mean standard error of the mean ranged between 4.0-7.6% for example month May 2010 (data not shown).

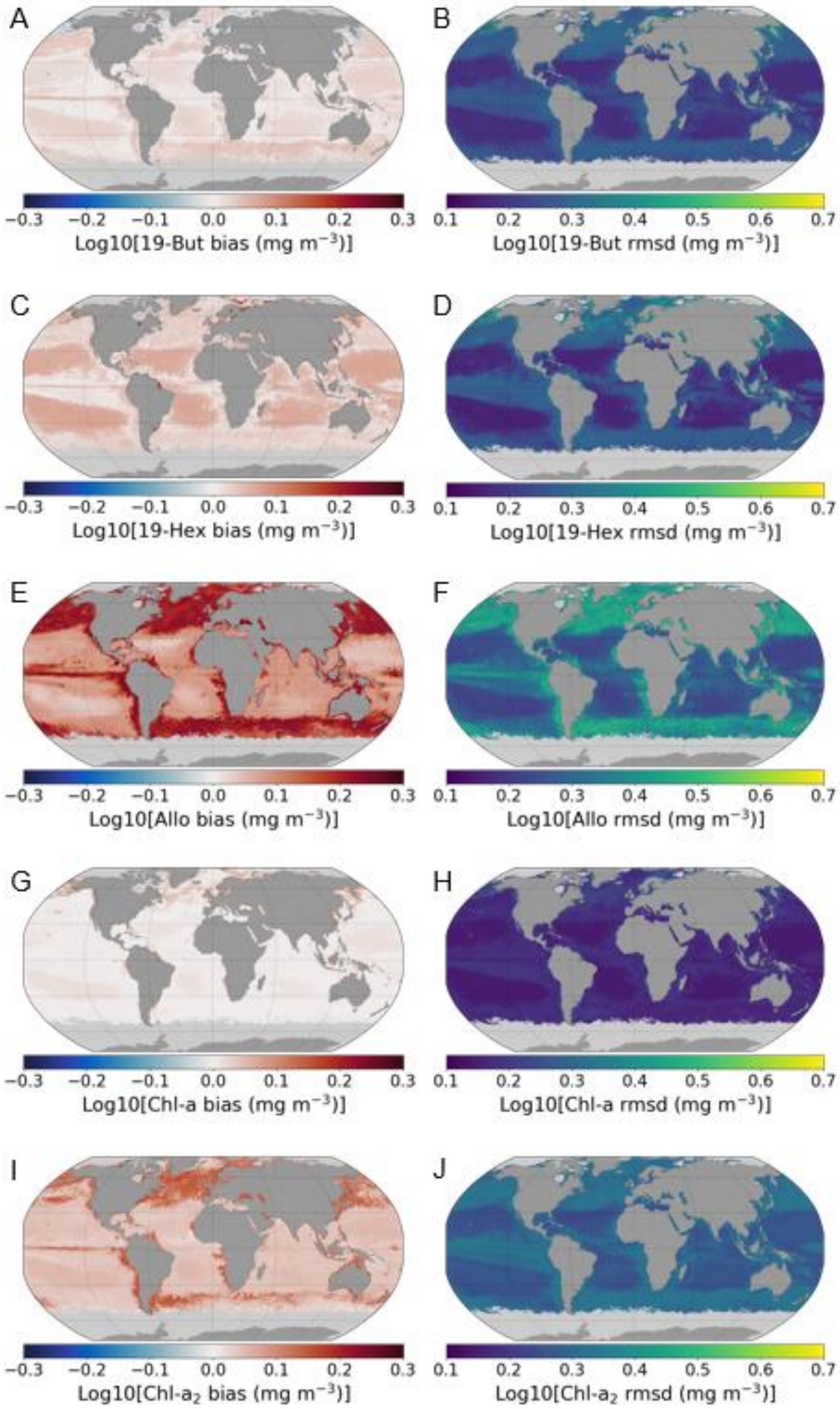

Figure 3. Example of bias and root-mean-square-difference (rmsd) in phytoplankton pigments from algorithm B_2 for May 2010. Bias and rmsd were assigned per-pixel using optical water types from OC-CCI using the information provided in Table 3. See Section 2 for a detailed description of the method. Abbreviations: 19-But = 19'-Butanoyloxyfucoxanthin, 19-Hex = 19'-Hexanoyloxyfucoxanthin, Allo = Alloxanthin, Chl-a = Total chlorophyll-a, Chl-a_2 = Divinyl chlorophyll-a, Chl-b = Total chlorophyll-b, Fuco = Fucoxanthin, Peri = Peridinin and Zea = Zeaxanthin.

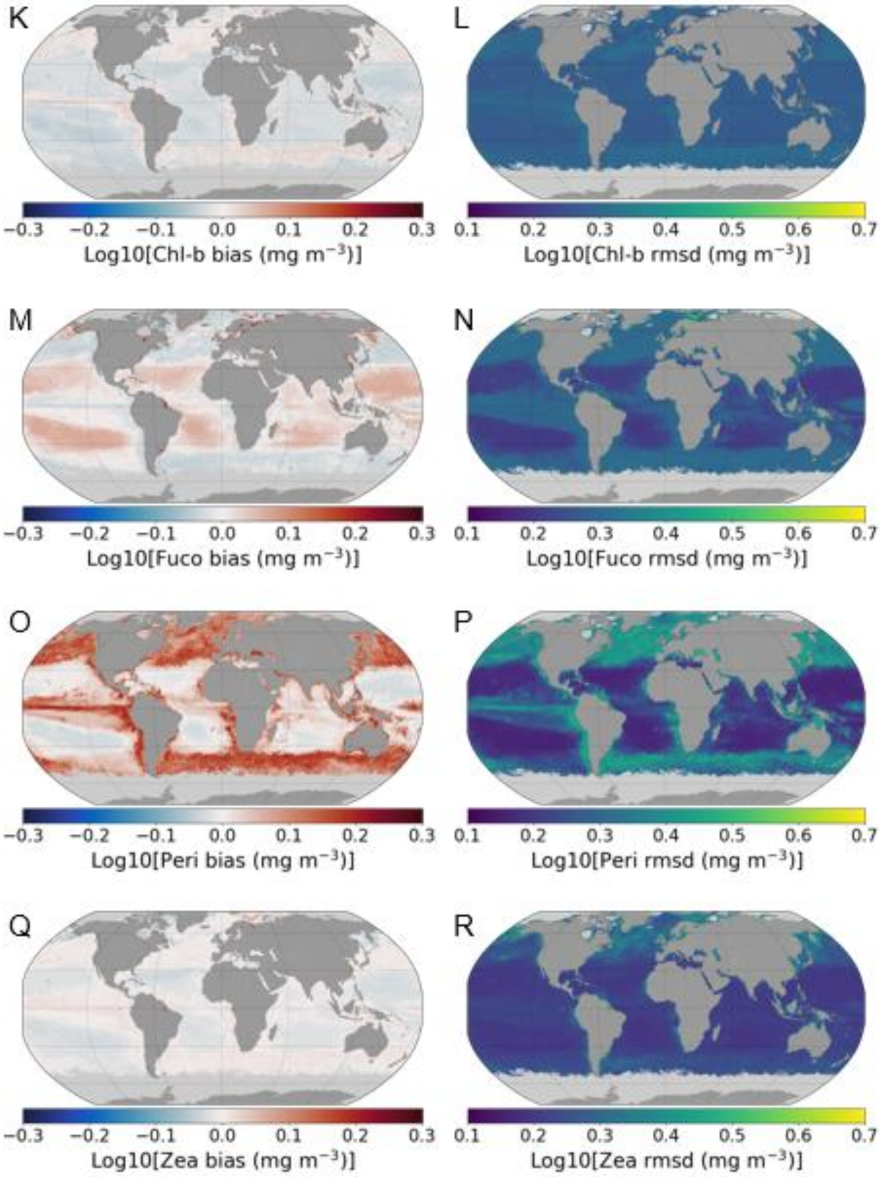

Figure 3. Continued.

4 Recommendations

The first version of the PHYTO-CCI dataset is provided with per-pixel uncertainties following the OWT approach, including mapped products of the bias and root-mean-square-difference in log10 scale. How these statistical metrics can be used to estimate the uncertainty in the data products, which requires information on the number of observations per pixel that is available from OC-CCI, is described in Section 2. Note that if the data is bias-corrected before use, the standard uncertainties have to be propagated following standard error propagation law (also see Section 2). The spatial patterns observed in example month May 2010 look as expected, with the error in the data product often proportional to the concentrations of phytoplankton carbon or the phytoplankton pigments. Higher relative errors are observed especially in the Southern Ocean in May 2010, and this is likely related to a lower number of ocean colour observations due to viewing angles in this month. We also note that assumptions were made for assigning uncertainties for some OWTs, for which insufficient *in situ* – satellite match-up data was available to estimate the bias and root-mean-square-difference. The impact of these assumptions should be further considered by the validation team and in the meantime care should be taken by users for these specific products and OWTs.

5 Outlook for future and further improvements

5.1 Formal uncertainty propagations

An approach for propagating radiometric data uncertainties through ocean colour algorithms was described by McKinna *et al.* (2019). Their paper "Approach for Propagating Radiometric Data Uncertainties Through NASA Ocean Color Algorithms" presents an application of the GUM uncertainty framework (first order first moment, FOFM) to propagate uncertainties from remote sensing reflectance through NASA's bio-optical algorithms. The FOFM calculations were validated by Monte Carlo simulations. The research utilised a dataset of 1,124 *in situ* hyperspectral spectra as a direct computational baseline. Because the original measurements were hyperspectral, they could also be precisely down sampled computationally to match the specific wavelength bands of satellite sensors.

PHYTO-CCI will follow the methodology of McKinna *et al.* (2019) in principle, but will use a dataset that is randomly sampled from the OC-CCI remote sensing reflectance product. One-hundred spectra will be sampled from each optical water class, in total 1,400 spectra. Unless the OC-CCI provides propagated remote sensing reflectance standard uncertainties, different uncertainty scenarios will be considered:

1) Spectrally uniform and uncorrelated relative standard uncertainties of one, five and ten percent of the measured remote sensing reflectance will be adopted as a proxy (McKinna *et al.*, 2019);
2) Spectrally-dependent uncorrelated standard uncertainties will be adopted as a proxy (McKinna *et al.*, 2019; Hu *et al.*, 2013); and/or
3) To model the unknown spectral variance-covariance, the spectral correlation matrix of each applicable optical water class will be scaled by the proxy standard uncertainties adopted in the previous scenarios.

Multiplying the proxy (or OC-CCI provided) standard uncertainties with the spectral correlation matrix of an OWT yields a mathematically consistent variance-covariance matrix. This procedure possesses high physical plausibility because atmospheric correction errors typically cascade across neighbouring wavelengths, and the water class matrix provides a realistic spectral coherence which, besides atmospheric correlations, reflects the natural variability of the water, too. To illustrate the planned activities, for the best-performing phytoplankton carbon algorithm (Algorithm C), we consider the spectral signatures of optical water classes (Table 4) and assume (as in the second scenario) relative standard uncertainty of 0.05 at wavebands 443, 490 and 510 nm, a relative standard uncertainty of 0.10 at 555 nm and a relative standard uncertainty of 0.20 at 670 nm (Hu *et al.*, 2013) and apply FOFM calculations to the Hu *et al.* (2019) Ocean Colour Index (OCI) algorithm that computes chlorophyll-a concentration from remote sensing reflectance, and the Marañón *et al.* (2014) empirical algorithm that computes phytoplankton carbon concentration from chlorophyll-a. Figure 4 and Table 4 illustrate the resulting mean values and standard uncertainties of the concentrations obtained by these algorithms. Moving forward, the planned activities will scale up this approach by considering 1,400 randomly sampled OC-CCI remote sensing spectra instead of only the 14 water class spectral signatures and will comprehensively incorporate all selected phytoplankton carbon biomass and pigment diversity algorithms.

Table 4. Typical values of chlorophyll-a and phytoplankton carbon biomass concentrations retrieved by the Hu et al. *(2019) OCI algorithm and the Marañón* et al. *(2014) algorithm, respectively, for each optical water type (OWT) spectral signature (corresponding to Figure 4).*

Typical values		
OWT	**$\log_{10} C_{chl}$ (mg m^{-3})**	**$\log_{10} C_{phy}$ (mg m^{-3})**
1	-1.66 (9)0	0.31 (8)0
2	-1.48 (8)0	0.47 (7)0
3	-1.31 (7)0	0.62 (6)0
4	-1.13 (7)0	0.78 (6)0
5	-0.96 (6)0	0.94 (5)0
6	-0.82 (6)0	1.06 (5)0
7	-0.74 (7)0	1.13 (7)0
8	-0.58 (8)0	1.28 (7)0
9	-0.29 (9)0	1.53 (8)0
10	-0.16 (10)	1.65 (9)0
11	-0.10 (13)	1.88 (11)
12	-0.71 (18)	2.43 (16)
13	-0.61 (17)	2.34 (15)
14	-0.63 (17)	2.35 (15)

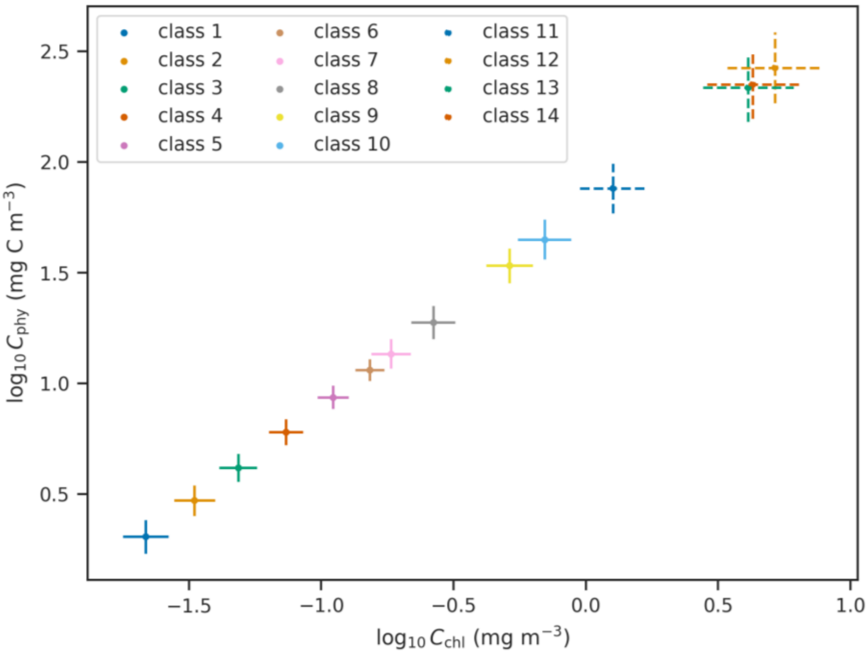

Figure 4. Typical values and uncertainties of chlorophyll-a (C_{chl}) and phytoplankton carbon (C_{phy}) concentrations retrieved by the Hu et al. (2019) OCI and the Marañón et al. (2014) algorithms, respectively, for each optical water class spectral signature. Estimates are based on the GUM uncertainty framework assuming spectrally uncorrelated errors and a relative remote sensing reflectance standard uncertainty of 0.05 at wavebands 443, 490 and 510 nm, a relative standard uncertainty of 0.10 at 555 nm and a relative standard uncertainty of 0.20 at 670 nm (Hu et al., 2013).

To gain a deeper understanding of how these uncertainties propagate through the models, the FOFM calculations inherently include the computation of sensitivities. Let $y = f(x)$ represent an algorithm f that computes an output y from an input x. Then the sensitivity of y with respect to a specific scalar input x_i is defined by the partial derivative:

$$c = \frac{\partial f}{\partial x_i}(x)$$

For quantities with different physical dimensions and units, it is more convenient to normalise sensitivities into dimensionless elasticities. This is achieved by multiplying a sensitivity with the ratio of x_i to y:

$$\epsilon = \frac{x_i}{y}\frac{\partial f}{\partial x_i}(x)$$

For instance, an elasticity of $\epsilon = 2$ implies that y would change by 2% if x_i were changed by 1%. Table 5 and Figure 5 below illustrate the spectral elasticity of phytoplankton carbon biomass concentration with respect to remote sensing reflectance across different water classes.

Table 5. Spectral elasticity of the combined empirical Marañón et al. *(2014) phytoplankton carbon biomass model and the Hu et al. (2019) OCI algorithm with respect to remote sensing reflectance for each optical water type (OWT) (corresponding to Figure 5).*

Elasticity of phytoplankton biomass model with respect to remote sensing reflectance					
OWT	**443 nm**	**490 nm**	**510 nm**	**555 nm**	**670 nm**
1	-3.215	-0.000	-0.000	0.723	-0.040
2	-2.828	-0.000	-0.000	0.708	-0.035
3	-2.510	-0.000	-0.000	0.732	-0.037
4	-2.173	-0.000	-0.000	0.770	-0.042
5	-1.830	-0.000	-0.000	0.793	-0.044
6	-1.560	-0.000	-0.000	0.812	-0.049
7	-2.110	-0.000	-0.000	1.078	-0.116
8	-1.831	-0.000	-0.000	1.427	-0.085
9	-1.613	-0.000	-0.000	1.613	-0.000
10	-0.000	-1.848	-0.000	1.846	-0.000
11	-0.000	-2.313	-0.000	2.313	-0.000
12	-0.000	-0.000	-3.301	3.301	-0.000
13	-0.000	-0.000	-3.151	3.151	-0.000
14	-0.000	-0.000	-3.176	3.176	-0.000

The resulting curves clearly reflect the dual nature of the OCI algorithm, which blends a maximum blue-to-green ratio chlorophyll algorithm with an RGB index algorithm. Specifically, elasticities in the blue wavebands (443, 490 and 510 nm) are anti-correlated with those in the green waveband (555 nm). Elasticity in the blue is negative, meaning that higher reflectance in the blue increases the blue-to-green ratio, thereby decreasing the retrieved chlorophyll-a and phytoplankton carbon biomasses. Conversely, elasticity in the green is positive, as higher reflectance in the green decreases the blue-to-green ratio and consequently increases the retrieved concentrations. Furthermore, the elasticity for blue wavebands that do not provide the maximum reflectance vanishes entirely due to the algorithm's maximum-selection logic. Elasticity for the red waveband at 670 nm is typically minuscule, since remote sensing reflectance at this wavelength is only considered for low-chlorophyll conditions within the colour-index as part of the algorithm.

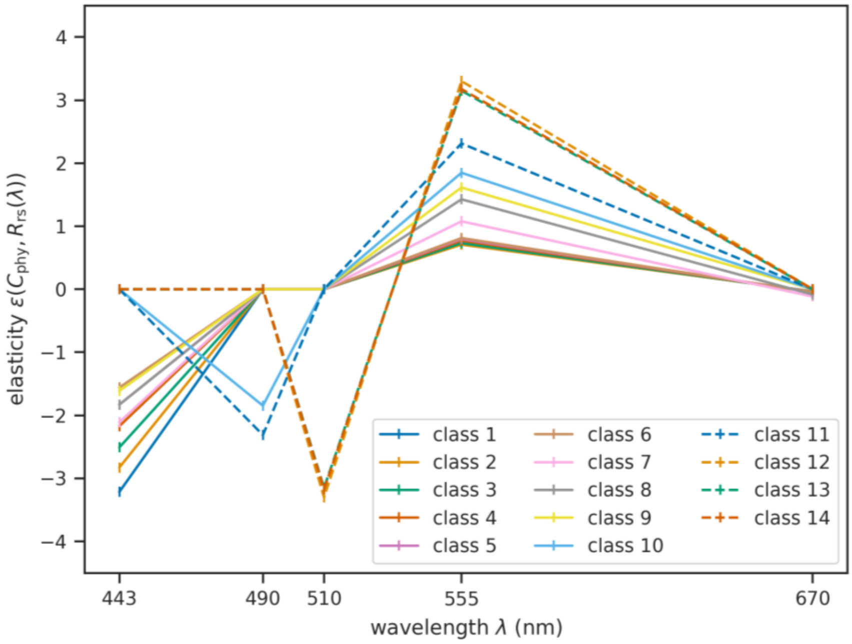

Figure 5. Spectral elasticity of the combined empirical Marañón et al. *(2014) phytoplankton carbon (C_{phy}) biomass algorithm and Hu* et al. *(2019) OCI algorithm with respect to remote sensing reflectance (Rrs), resolved for each optical water class.*

As in McKinna *et al.* (2019), FOFM calculations will be validated with Monte Carlo simulations. For algorithms where FOFM calculations are not feasible, only Monte Carlo simulations will be conducted to establish the uncertainty budget.

5.2 Sources of uncertainty

FOFM and Monte Carlo uncertainty propagation methods are not specific to a certain source or type of uncertainty. Every source of uncertainty can be propagated from input to output separately and independent of any additional source of uncertainty. Table 6 below lists the sources of uncertainty ESA PHYTO-CCI can consider. All upstream sources of uncertainty like, e.g., radiometric sensor noise, calibrations errors or retrieval errors can only be considered upstream, i.e., by ESA OC-CCI, the products of which constitute the main input to PHYTO-CCI. Once quantified upstream, PHYTO-CCI can propagate all of them downstream (in principle) by means of FOFM and Monte Carlo methods.

Table 6. Sources of uncertainty considered by ESA PHYTO-CCI.

Source of Uncertainty	Operational Origin	Quantification	Downstream budget
What type of uncertainty is the cause?	**Where is the uncertainty quantified?**	**How is the uncertainty quantified?**	**How is it budgeted downstream?**
Representation uncertainty of ESA OC-CCI products when compared to *in situ* measurements	ESA OC-CCI products	Combined bias and RMSD in comparison to *in situ* measurements (OWT approach)	Not relevant for ESA PHYTO-CCI. This uncertainty is localised to the *in situ* comparison interface and is not applicable to PHYTO-CCI downstream processing, which stays in the remote sensing context.
Uncertainty of ESA OC CCI inputs propagated to OC-CCI products (upstream)	Expressed formally in the ESA OC-CCI E3UB document. Quantified in the ESA OC-CCI E3UB for a limited sample of data on four specific sites.	Quantified in terms of standard uncertainty for a limited sample of data on four specific sites.	ESA PHYTO-CCI demonstrates propagation of ESA OC-CCI uncertainty by means of FOFM and Monte Carlo methods on a representative sample of 1,400 remote sensing reflectance spectra. Unless ESA OC-CCI provides propagated remote sensing reflectance uncertainty for these samples, PHYTO-CCI makes ad hoc assumptions.
Intrinsic uncertainty of ESA OC-CCI algorithms (upstream)	Not quantified.	Not quantified.	Once quantified, ESA PHYTO-CCI could propagate ESA OC-CI algorithm uncertainty by means of FOFM and Monte Carlo methods.

Table 6. Continued.

Source of Uncertainty	**Operational Origin**	**Quantification**	**Downstream budget**
What type of uncertainty is the cause?	**Where is the uncertainty quantified?**	**How is the uncertainty quantified?**	**How is it budgeted downstream?**
Representation mismatch of ESA PHYTO-CCI products when compared to *in situ* measurements	ESA PHYTO-CCI products	Combined bias and RMSD in comparison to *in situ* measurements (OWT approach)	Quantified operationally at the product's specific comparison interface.
Intrinsic uncertainty of ESA PHYTO-CCI algorithms	Unknown	Unknown	ESA PHYTO-CCI algorithms consist of empirical models with parameters fit to observational data, often using a methodology that does not provide uncertainty. Parameter uncertainty can be quantified by repeating the fit with appropriate methodology and then be propagated by means of FOFM or Monte Carlo methods.
Uncertainty of auxiliary data used by ESA PHYTO-CCI	Unknown	Unknown	Once quantified, ESA PHYTO-CCI can propagate uncertainty of auxiliary data to PHYTO-CCI products by means of FOFM or Monte Carlo methods.

Propagated uncertainty is sometimes referred to as prognostic uncertainty. Propagated uncertainty describes a purely mathematical mechanism. It is the process of passing input errors through a function, algorithm, or model to see how they multiply or compound at the output. It is governed by calculus (e.g., FOFM or Monte Carlo simulations). Prognostic uncertainty describes an operational intent. "Prognostic" means to predict (or forecast) the (future) state of a system and all uncertainty (not only propagated uncertainty) can be prognostic (even representation uncertainty). The strict metrological term is propagated uncertainty.

6 References

Bellacicco, M., Pitarch, J., Organelli, E., Martinez-Vicente, V., Volpe, G., & Marullo, S. (2020). Improving the Retrieval of Carbon-Based Phytoplankton Biomass from Satellite Ocean Colour Observations. Remote Sensing, 12(21), 3640. https://doi.org/10.3390/rs12213640

Bulgin, C. E., Thomas, C. M., Waller, J. A., & Woolliams, E. R. (2022). Representation uncertainty in the Earth sciences. Earth and Space Science, 9(6). https://doi.org/10.1029/2021ea002129

Hu, C., Feng, L., & Lee, Z. (2013). Uncertainties of SeaWiFS and MODIS remote sensing reflectance: Implications from clear water measurements. Remote Sensing of Environment, 133, 168–182. https://doi.org/10.1016/j.rse.2013.02.012

Hu, C., Feng, L., Lee, Z., Franz, B. A., Bailey, S. W., Werdell, P. J., & Proctor, C. W. (2019). Improving satellite global Chlorophyll A data products through algorithm refinement and data recovery. Journal of Geophysical Research Oceans, 124(3), 1524–1543. https://doi.org/10.1029/2019jc014941

Jackson, T., Sathyendranath, S., & Mélin, F. (2017). An improved optical classification scheme for the Ocean Colour Essential Climate Variable and its applications. Remote Sensing of Environment, 203, 152–161. https://doi.org/10.1016/j.rse.2017.03.036

JCGM (2023). Guide to the expression of uncertainty in measurement — Part 1: Introduction. https://doi.org/10.59161/jcgmgum-1-2023

Kostadinov, T. S., Lain, L. R., Kong, C. E., Zhang, X., Maritorena, S., Bernard, S., Loisel, H., Jorge, D. S. F., Kochetkova, E., Roy, S., Jonsson, B., Martinez-Vicente, V., & Sathyendranath, S. (2023b). Ocean color algorithm for the retrieval of the particle size distribution and carbon-based phytoplankton size classes using a two-component coated-sphere backscattering model. Ocean Science, 19(3), 703–727. https://doi.org/10.5194/os-19-703-2023

Li, X., Li, X., Yang, Y., Ishizaka, J., Li, X., & Li, X. (2023). Global estimation of phytoplankton pigment concentrations from satellite data using a deep-learning-based model. Remote Sensing of Environment, 294, 113628. https://doi.org/10.1016/j.rse.2023.113628

Marañón, E., Cermeño, P., Huete-Ortega, M., López-Sandoval, D. C., Mouriño-Carballido, B., & Rodríguez-Ramos, T. (2014). Resource supply overrides temperature as a controlling factor of marine phytoplankton growth. PLoS ONE, 9(6), e99312. https://doi.org/10.1371/journal.pone.0099312

McKinna, L. I. W., Cetinić, I., Chase, A. P., & Werdell, P. J. (2019). Approach for propagating radiometric data uncertainties through NASA ocean color algorithms. Frontiers in Earth Science, 7, 176. https://doi.org/10.3389/feart.2019.00176

Sathyendranath, S., Platt, T., Kovač, Ž., Dingle, J., Jackson, T., Brewin, R. J. W., Franks, P., Marañón, E., Kulk, G., & Bouman, H. A. (2020). Reconciling models of primary production and photoacclimation [Invited]. Applied Optics, 59(10), C100. https://doi.org/10.1364/ao.386252

Yang, G., Bellacicco, M., Organelli, E., & Xing, X. (2024). Global variability of phytoplankton carbon and Non-Algal particles from ocean color data based on a photoacclimation model. Journal of Geophysical Research Oceans, 129(1). https://doi.org/10.1029/2023jc019922